Chinese Chemical Letters 35 (2024) 109536

Contents lists available at ScienceDirect

Chinese Chemical Letters

journal homepage: www.elsevier.com/locate/cclet

Unraveling the chemical and structural evolution of novel Li-rich layered/rocksalt intergrown cathode for Li-ion batteries

Yongjian Li[a,b], Xinyu Zhu[a,b], Chenxi Wei[c], Youyou Fang[a,b], Xinyu Wang[a,b], Yizhi Zhai[a], Wenlong Kang[a], Lai Chen[a,b], Duanyun Cao[a,b], Meng Wang[b], Yun Lu[a,b], Qing Huang[a,b], Yuefeng Su[a,b,*], Hong Yuan[a,d,*], Ning Li[a,b,*], Feng Wu[a,b]

[a] School of Materials Science and Engineering, Beijing Key Laboratory of Environmental Science and Engineering, Beijing Institute of Technology, Beijing 100081, China
[b] Chongqing Innovation Center, Beijing Institute of Technology, Chongqing 401120, China
[c] Center for Transformative Science, ShanghaiTech University, Shanghai 201210, China
[d] Advanced Research Institute of Multidisciplinary Science, Beijing Institute of Technology, Beijing 100081, China

ARTICLE INFO

Article history:
Received 8 December 2023
Revised 27 December 2023
Accepted 11 January 2024
Available online 19 January 2024

Keywords:
Cathode materials
Intergrown structure
Cationic-anionic redox
Low strain
Synchrotron characterizations

ABSTRACT

The prototype material, $Li_{1.23}Ru_{0.41}Ni_{0.36}O_2$, is proposed to gain the deep and comprehensive understanding of chemical and structural changes of the novel layered/rocksalt intergrown cathodes. Synchrotron-based X-ray absorption spectra and resonant inelastic X-ray scattering reveal that both cationic and anionic redox evolves in the charge compensation process of the intergrown material, while synchrotron-based extended X-ray fine structure spectra and *in situ* X-ray diffraction measurements demonstrates that the intergrown material undergoes minimal local- and long-range structural variations at deep de/lithiation. This work highlights the great potential of the intergrown structure to inspire the design of advanced cathode materials for lithium-ion batteries.

High-capacity cathode materials are currently crucial for elevating the energy density of lithium-ion batteries in the application of laptop devices, electric vehicles as well as smart grids. Li-excess layered cathode materials have gained widespread attention, due to the extra activation of unique oxygen anionic couple (O^{n-}/O^{2-}) besides the transition metal (TM) redox, in comparison with the commercialized cathode materials, such as $LiCoO_2$, NMC and $LiFePO_4$ [1–7]. However, the challenges of those high-capacity cathodes impede their actual applications, and all these layered cathodes face the dilemma that the high-capacity and high-structural stability cannot be achieved at the same time, especially the obvious capacity decay at elevated voltage windows and the anisotropy-induced structural collapse under deep lithium deintercalation [8–11].

Tremendous efforts have been devoted to balancing the capacity and structural stability of these layered cathode materials, especially to focus on the modification strategies for enhancing the structural integrity near the surface/interface. Among these modifying methods, surface coating and elemental doping are widely reported in the literatures [12,13]. The electrochemical active/inactive oxides (Al_2O_3, ZnO, ZrO_2), polyanionic materials, carbon and organic polymers mainly serve as a physically protective layer to prevent parasitic reactions between surface and electrolytes as well as surface gas evolution and densification [14–17]. In addition, elemental doping including metallic and non-metallic elements is also employed into the Li slab or TM slab as well as the oxygen matrix to further stabilize the bulk structure and mitigate structural collapse after deep delithiation [18–21]. However, the modification on the surface and bulk structure still has limitations by the doping and coating methods, and the modified material cannot hold the structural stability for long-term, fast and high-voltage cycling.

Recently, structural design by phase-compatible strategies have also been proposed to stabilize the bulk structure of the high-capacity layered cathodes, as these compatible phases have similar cubic close-packed oxygen matrix but different TM occupancies [22–24]. Our group prepared spinel epitaxial layered Li-rich manganese materials with fast Li^+ diffusion pathways, showing outstanding capacity and rate performance [25,26]. Lu *et al.* introduced a coherent perovskite phase to Ni-rich cathode materials, significantly reducing lattice strain and leading to notable improvements in cycling stability [27]. Li *et al.* investi-

* Corresponding authors.
E-mail addresses: suyuefeng@bit.edu.cn (Y. Su), yuanhong@bit.edu.cn (H. Yuan), ningli@bit.edu.cn (N. Li).

https://doi.org/10.1016/j.cclet.2024.109536
1001-8417/

gated an intergrowth material with layered $LiNiO_2$-based domains and cationic disordered rocksalt Li_4MoO_5-base domains, which showed much improved cycling performance [28]. Meanwhile, we have developed a series of layered-rocksalt intergrown cathodes with uniform distribution of two phases, and among them, $Li_{1.2}Ni_{0.4}Ru_{0.4}O_2$ model cathode showing nearly zero-strain isotropic structural evolution at deep (de)insertion [29]. Low-cost Li-rich $Li_{1.2}Ru_{0.2}Mn_{0.3}Ni_{0.3}O_2$ cathode has been proposed to display ultrahigh Li ions (de)insertion (1.11 Li^+ removal and 0.87 Li^+ insertion) and extremely low-strain operation [23]. The amalgamation of the high-performance single-phase cathode within an intergrown material show a highly promising avenue for the exploration of advanced battery cathodes, while a deeper and better understanding of the work mechanism is still needed for those novel Li-rich layered-rocksalt intergrown materials.

Herein, initiated by employing a prototype material $Li_{1.23}Ru_{0.41}Ni_{0.36}O_2$ based on Ni^{2+} and Ru^{5+} combination, we systematically elucidate the chemical and structural changes occurring during the charge-discharge cycles by combination with Cs-corrected STEM, hard X-ray absorption spectra, resonant inelastic X-ray scattering, and *in-situ* X-ray diffraction. It is found that Ni and anionic O are involved in charge compensation during cycling, while the Ru^{5+} in the intergrown material remains unchanged [29]. The data demonstrate that the bulk and local structural of the as-prepared intergrown material only shows slight variations during cycling, further demonstrating the structural advantage of the intergrown cathode. The insights should provide an enhanced understanding of the charge and discharge mechanisms and unique low-strain structural evolution in the novel intergrown cathode material, and it is hoped this work should guide the future design of advanced cathode material for lithium-ion batteries.

Fig. 1a shows the scanning electron microscopy (SEM) image of $Li_{1.23}Ru_{0.41}Ni_{0.36}O_2$ material prepared by the solid-state method. It can be seen that the as-prepared powders have an ordered angular shape with average particle sizes of 1.5–2.0 μm. Figs. 1b-e show the energy disperse spectroscopy (EDS) images of the as-prepared material, and all the elements, O, Ni and Ru, are dispersed uniformly within the as-prepared material. To observe the atomic microstructure of $Li_{1.23}Ru_{0.41}Ni_{0.36}O_2$, high-angle annular dark field-scanning transmission electron microscopy (HAADF-STEM) has been employed to directly visualize the atomic distribution of TM, and the most representative HAADF-STEM image of the as-prepared material is shown in Fig. 1f. HAADF-STEM image reveals that there are two typical crystalline zones interweaved within the particles, the layered domain arrangement of TM ions on the right (highlighted by the red square) and the rocksalt domain on the left (highlighted by the orange square). There is no obvious particle boundary between layered and rocksalt domains, but naturally transiting with an intermediate phase. The enlarged views of the rocksalt, intermediate, and layered phases are shown in Figs. 1g-i, respectively. The apparently different arrangements of Li^+ and TM ions can be identified in these three regions. In the layered structure area, the Li and TM ions are arranged in an orderly manner, consisting of adjacent slabs of bright spots and dark spots, while in the rocksalt structure area, the Li and TM ions are randomly distributed, showing an obviously disordered state. Thus, the HAADF-STEM data clearly reveals the as-prepared material has a layered/rocksalt intergrown structure.

To further confirm the intergrown structure of pristine $Li_{1.23}Ru_{0.41}Ni_{0.36}O_2$, the X-ray diffraction (XRD) characterization is utilized (Fig. 1j). All the reflections can be indexed well with both layered $R\bar{3}m$ structure and rocksalt $Fm\bar{3}m$ structure as observed in Fig. 1j. It is worth noting that the super-lattice peaks around the 2θ region of 18°−23°, which is always seen in conventional layered Li-rich cathode materials, can be hardly seen, which may be due to the absence of Li/TM ordering in the TM slabs of layered phase in the as-prepared material. Rietveld refinement of XRD is further been carried out based on the $R\bar{3}m$ and $Fm\bar{3}m$ biphasic models for the as-prepared material. The refinement result is shown in Tables S1 and S2 (Supporting information), and it shows that there is 78.6 mol% layered phase and 21.4 mol% rocksalt phase in the as-prepared material. Therefore, combined with XRD and HAADF-STEM analysis, the as-prepared material shows a distinct layered/rocksalt intergrown structure. The chosen transition metals play a critical role in formation of the intergrown structure, and the combination of Ni^{2+} (0.69 Å) and Ru^{5+} (0.57 Å, $4d^3$) in the Li-rich oxides is verified to be feasible to form layered-rocksalt intergrown structure [29]. The Ni^{2+} ions with radical size similar to Li^+, tend to partially intermix with Li^+ and occupy the Li^+ octahedral sites, while the Ru^{5+} ions with distortable d^3 electronic configuration, are feasible to accommodate complex octahedral environments of both layered and rocksalt structures.

To investigate the electrochemical advantages of the as-prepared intergrown material, the electrochemical performance of the intergrown cathode $Li_{1.23}Ru_{0.41}Ni_{0.36}O_2$ has been measured in galvanostatic mode with two different voltage window at 2.5–4.6 V and 2.0–4.8 V at current density of 12.5 mA/g. The initial charge-discharge profiles in Fig. 2a show that the intergrown cathode exhibits superior lithium ions storage capability with 0.98 Li^+ deintercalation on initial charge and 0.81 Li^+ intercalation during subsequent discharge at the voltage window of 2.5–4.6 V, while it dis-

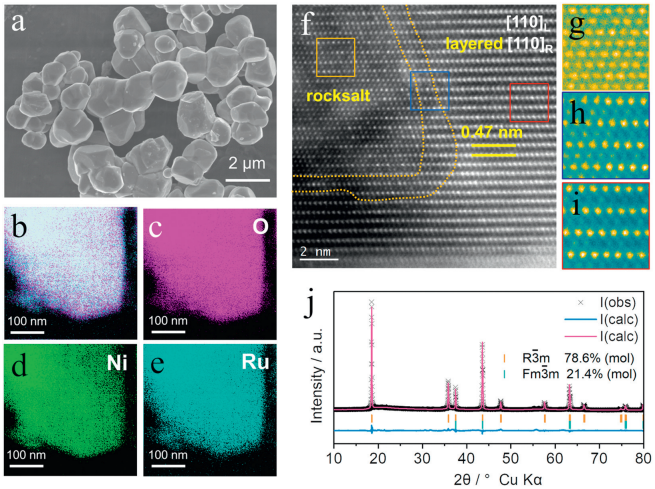

Fig. 1. Morphologies and structural characterization of intergrown $Li_{1.23}Ru_{0.41}Ni_{0.36}O_2$ material. (a) SEM images for pristine powder. Elemental mapping of (b) overall, (c) O, (d) Ni and (e) Ru. (f) STEM-HAADF image and (g) magnified patterns for orange square, (h) blue square and (i) red square. (j) Biphase-based Rietveld refinement profiles using the $R\bar{3}m$ and $Fm\bar{3}m$ models.

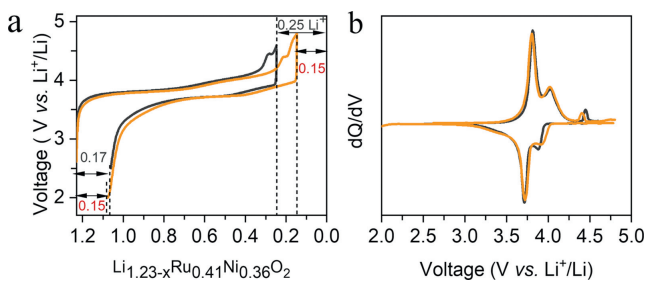

Fig. 2. Electrochemical characterization of intergrown $Li_{1.23}Ru_{0.41}Ni_{0.36}O_2$ material. (a) The initial charge-discharge voltage profiles and (b) corresponding d*Q*/d*V* curves between 2.5–4.6 V and 2.0–4.8 V. The electrochemical test has been conducted with current density of 12.5 mA/g.

plays ultrahigh Li^+ extraction of 1.03 of 1.23 total Li inventory and superior reversible Li^+ reinsertion of 0.93 at voltage window of 2.0–4.8 V. Interestingly, this material shows an additional capacity contribution beyond the fully activated and reversible cationic redox (~0.72 e^-), implying the anionic redox for the charge compensation that occurs during electrochemical cycling.

To identify the detailed electrochemical contribution during charge and discharge, the corresponding d*Q*/d*V* curves of the as-prepared materials are shown in Fig. 2b. The intergrown cathode clearly presents two highly reversible redox peaks and one irreversible anodic peak, which is probably associated with the parasitic reactions with electrolytes. To distinguish the redox capacity contribution within the different electrochemical windows, we also conducted a series of electrochemical test by gradually changing the charge and discharge cutoff voltage. The detailed electrochemical curves are shown in Figs. S1a and b (Supporting information). The corresponding d*Q*/d*V* curves in Figs. S1c and d (Supporting information) are almost overlapped at different voltage windows, which further confirm the high reversible electrochemical redox reactions in the as-prepared intergrown cathode material. Interestingly, there is no apparent voltage hysteresis in the d*Q*/d*V* curves which is commonly seen in both layered and rocksalt Li-rich materials. The voltage hysteresis in both layered and rocksalt Li-rich materials are mainly ascribed to the dynamically irreversible anionic oxygen redox. Hence, the electrochemical data demonstrates some kinds of contradiction that the Li storage capability of the intergrown cathode indicates the extra anionic redox contribution beyond the cationic redox, while the d*Q*/d*V* curves manifest that there is no clear evidence targeted for "dynamically irreversible" anionic oxygen redox. Therefore, a deep and comprehensive analysis of the charge compensation process is needed to interpret the outstanding Li storage capability of the as-prepared intergrown cathode material.

To gain a better understanding of the fundamental redox processes occurring within the $Li_{1.23}Ru_{0.41}Ni_{0.36}O_2$ cathode material during charge and discharge, the charge compensation mechanism of the intergrown cathode $Li_{1.23}Ru_{0.41}Ni_{0.36}O_2$ was elucidated by combining hard X-ray absorption spectroscopy (hXAS) and resonant inelastic X-ray scattering (RIXS) for the oxygen state in bulk. Figs. 3a and b show Ru *K*-edge and Ni *K*-edge hXAS at five representative SOCs based on the initial d*Q*/d*V* curves. Fig. 3c shows the variation of the threshold energy position of TM *K*-edge, which is the half-edge energy ($E_{0.5}$) deduced by the half-height method [30]. It can be seen the energy of Ru and Ni at half maxima is consistent with Ru^{5+} and Ni^{2+} reference, which further verifies our previous principle to design intergrown cathode. When charging to 3.9 V, the $E_{0.5}$ of Ru *K*-edge maintains unchanged, while the $E_{0.5}$ of Ni *K*-edge shifts to its highest value, implying the dominant charge compensation from Ni element below 3.9 V for the intergrown cathode. When further charging to 4.6 V, the $E_{0.5}$ of both Ni *K*-edge and Ru *K*-edge does not increase but shifts to a lower value, and this phenomenon is commonly reported in anionic oxygen activities of Li-rich oxides, which is associated with the ligand-metal charge transfer between the oxygen and surrounding coordinated TM ions [31–33]. When the discharge voltage reaches 3.8 V, the $E_{0.5}$ of both Ni *K*-edge and Ru *K*-edge remains unchanged, indicating that no TM reduction but anionic oxygen reduction involves charge compensation above 3.8 V discharging. Further discharging to 2.5 V, the $E_{0.5}$ of Ru *K*-edge changes slightly, indicating that Ru nearly does not involve the charge compensation process at the initial cycle, as the Ru^{5+} is not easily further oxidized under typical battery operating conditions, while the Ru^{5+} with distortable d^3 electronic configuration, may act as a structural stabilizer for both layered and rocksalt phase within the intergrown material, possibly contributing to the overall structural and electrochemical stability. While the $E_{0.5}$ of Ni *K*-edge shifts back to the pristine state, implying the highly reversible Ni redox reaction in the as-synthesized intergrown cathode.

Moreover, the valence change of anionic oxygen is probed by RIXS, as RIXS offers unique advantages over XPS and O K-edge soft XAS in the detection depth and characterization principle. RIXS is capable of differentiating the intrinsic oxidized oxygen signals from the dominating TM characters along the new dimension of emission energy. RIXS could resolve the emission out fluorescence photons energy in the single data plot, encompassing not just the excitation of core electrons (O 1s) to unoccupied states above the Fermi level, but also the release of photons by electrons from the occupied valence states beneath the Fermi level as they revert to the core-hole states at depths of up to 150 nm into the sample, in comparison with only photons counts from soft XAS at a con-

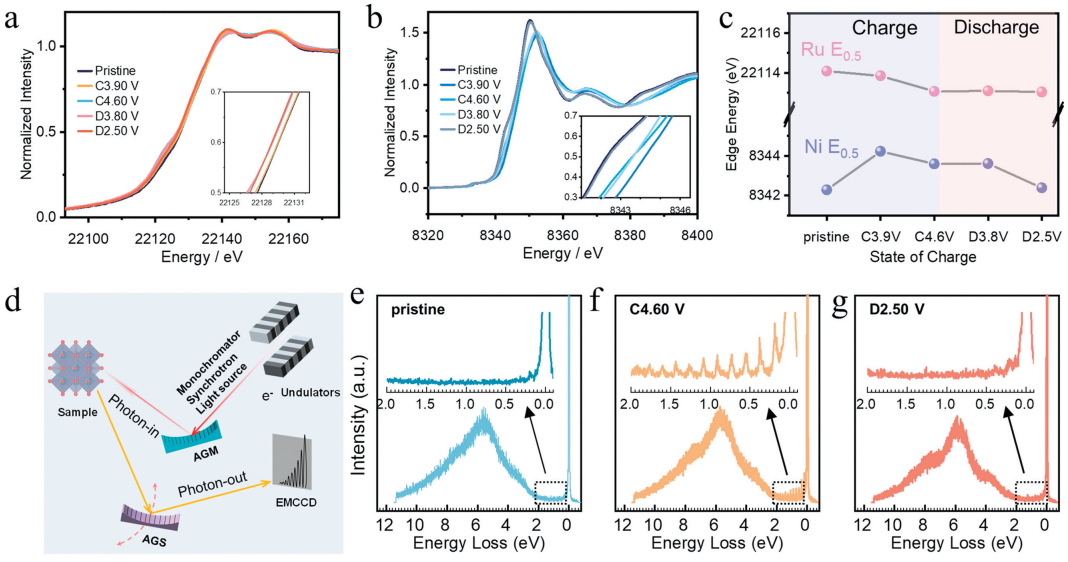

Fig. 3. Cationic redox and anionic oxygen redox of $Li_{1.23}Ru_{0.41}Ni_{0.36}O_2$ material during the initial cycle. (a) Ru *K*-edge XANES and (b) Ni *K*-edge XANES at different electrochemical states. (c) Corresponding edge energy $E_{0.5}$ for Ru and Ni *K*-edge XANES. (d) The schematic diagram of RIXS measurement. The O *K*-edge RIXS spectra collected at an excitation energy of 531 eV (e) at pristine, (f) charging to 4.6 V and (g) discharging to 2.5 V. The inset corresponds to the enlargement features near the elastic peak (the energy loss is zero).

stant incident energy. Fig. 3d displays the schematic illustration of RIXS measurement. Figs. 3e-g show the RIXS line scans of the intergrown cathode at a constant excitation energy of ~531 eV at pristine state, charging to 4.6 V and discharging to 2.5 V, and all the scans show a similar elastic peak at the energy loss of 0 eV, and a broadened peak at ~6 eV which is attributed to the strong hybridization between TM-O. Most importantly, for the sample at 4.6 V charging, a series of sharp peaks emerge close to the elastic peak between 0 and 2 eV, which has been reported previously to be associated with the molecular O_2 gas, or oxidized oxygen [34,35]. This feature disappears at 2.5 V discharging, indicating the highly reversible anionic oxygen redox in the intergrown cathode. Thus, combined with both hXAS and RIXS results, we can find that the Ni mainly oxidized below 3.9 V and then anionic oxygen oxidized during charging, and during discharging, oxygen reduced mainly above 3.8 V, and then Ni reduced to pristine state at 2.5 V. Both cationic and anionic redox displays superior reversibility and enables the intergrown material yield outstanding Li-ion storage capability during charge and discharge.

As maintaining structural integrity while achieving high energy density remains a great challenge for current cathode material, *in situ* XRD analysis has been conducted on the intergrown material $Li_{1.23}Ru_{0.41}Ni_{0.36}O_2$ with superior reversible lithium storage capability. The whole 2D contour plot of *in situ* XRD patterns collected from 15° to 70° (2θ) and the corresponding charge/discharge curves of the initial cycles are shown in Fig. 4a and Fig. S2 (Supporting information), respectively. Figs. 4b-d display the 2D contour plots for (003), (101) and (104) plane diffraction peaks based on the layered phase index, which are closely associated with interlayer spacing and in-plane atomic arrangements. The intergrown material presents a continuous shift of diffraction peak with slight peak broadening, implying the compatibility between layered and rocksalt phase. Figs. 4e and f present variations of the calculated lattice parameters *c* and *a*. Obviously, both lattice parameters *c* and *a* display only slight expansion/contraction of 0.65% and 1.8% during cycling. More importantly, both parameters shift back to the pristine state at the end of discharge, further demonstrating the reversible and low-strain long-range structural evolution of the intergrown material. The main layered phase in intergrown structure presents much less structural change compared with the conventional Li-rich layered materials, indicating the interweaved rocksalt phase may effectively suppress it.

To further analyze the origin of superior structural stability of $Li_{1.23}Ru_{0.41}Ni_{0.36}O_2$ material and decouple the effect from layered with all diffraction peak overlapping with rocksalt phase, the *R* space plots obtained from the Fourier transform of the *k*-weighted (k^2) Ru and Ni *K*-edge EXAFS spectra have been shown in Figs. 4g and h, to analyze the local-ordering structural evolution. Notably, the actual bond length would be longer than the *R* value due to the phase shifts ($\delta(k)$) in the EXAFS in Figs. 4i and j. It can be seen the Ni-O bond contracts when charged to 3.8 V, expanding at the end of charge, and remaining steady above 3.8 V discharging and shifting back to the pristine state at the end of discharge. This variation of Ni-O bond is in well agreement with the valence change of Ni in Fig. 3b. Meanwhile, the length of Ru-O and Ni-O bonds changes slightly, consisting with the low-strain long-range structural change of the as-prepared intergrown material. Furthermore, the local Ni-O and Ru-O bond lengths present the same tendency, but the latter shows less degree at the initial cycle, which also decrease the anisotropic change and enhance the

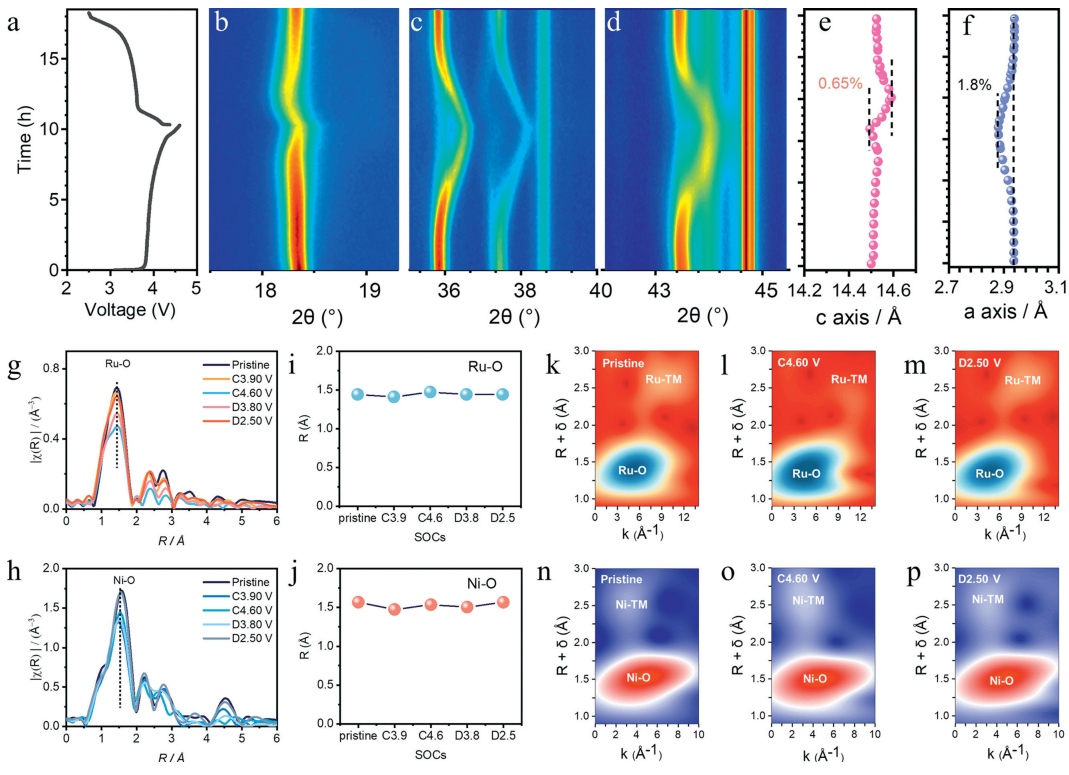

Fig. 4. Structural evolution of intergrown $Li_{1.23}Ru_{0.41}Ni_{0.36}O_2$ material during the initial cycle. *In situ* lab-XRD characterization on the structural evolution during the first charge/discharge at the voltage window between 2.5–4.6 V. (a-d) The electrochemical curve and corresponding enlarged 2D contour plots of Bragg peaks from (003), (101), (104) plane based on $R\bar{3}m$ space group, respectively. (e, f) Evolution of the lattice parameters *c* and *a* during charge/discharge. (g) R space plot from Ru *K*-edge extended X-ray absorption fine structure (EXAFS) spectra and (i) corresponding Ru-O bond lengths, and corresponding wavelet transform for (k) the pristine, (l) charging to 4.6 V and (m) discharging to 2.5 V. (h) R space plot from Ni *K*-edge EXAFS spectra and (j) corresponding Ni-O bond lengths, and corresponding wavelet transform for (n) the pristine, (o) charging to 4.6 V and (p) discharging to 2.5 V.

structural stability at various charge/discharge state, guaranteeing better structural compatibility.

In addition, the wavelet transform (WT) of EXAFS data combining both radial and *k*-space (frequency) information is used to characterize the local structural environment around Ni and Ru elements as illustrated in Figs. 4k-p. It can be seen in Figs. 4k-m that the bond lengths of approximately 1.4 and 2.7 Å correspond to Ru-O and Ru-TM bonds respectively, while the bond lengths of approximately 1.5 and 2.5 Å in Figs. 4n-p represent Ni-O and Ni-TM bonds. The almost unchanged WT Ru and Ni *K*-edge EXAFS results for the pristine and discharged 2.5 V also support the reversible local-ordering structural evolution. Although Ni ions serve as the dominant redox-active cationic centers, the WT analysis reveals superior stability in the Ni-O and second coordination shell Ni-TM structures during charge and discharge in comparison with that of Ru, which is quite different from widely reported results where redox-active metal ions exhibit significant changes in their local coordination environment [36]. Interestingly, the first coordinated shell Ru-O and second-coordinated Ru-TM for the charged state of 4.6 V presents notable change in comparison with the pristine state, which is well consistent with the change of coordination intensity in the *R* space plot in Fig. 4g. This distinction might stem from the electrochemical activation of oxygen ions. Upon charging to 4.6 V, the oxygen ions oxidation would lead to a shortening of O–O bond lengths and the formation of O–O dimers, and consequently, Ru with much stronger covalence with oxygen would undergo considerable coordination environment changes to accommodate the change of local lattice oxygen anions, which is also consistent with the valence change of Ru in Fig. 3a. This finding may provide deep insights into the correlation between the anionic oxygen redox and the local structural evolution, and provide more guidance for optimizing the electrochemical performance and stability of these advanced cathode materials.

In summary, layered-rocksalt intergrown $Li_{1.23}Ru_{0.41}Ni_{0.36}O_2$ material was successfully prepared and characterized by Cs-corrected STEM-HAADF. It exhibits superior lithium ions (de)lithiation capability with 1.08 Li^+ deintercalation on charge and 0.93 Li^+intercalation on discharge. The hXAS and RIXS reveal that both anionic and cationic redox reactions participate in the charge compensation process. The low-strain long-range structural evolution during the initial cycle was demonstrated by *in-situ* XRD, which is much less than traditional layered cathode materials. WT analysis further showed that Ni ions presents a relatively stable coordination environment, while the Ru undergoes much bigger local environmental change due to strong covalence to anionic lattice oxygen. Our study shows a significant and comprehensive understanding on chemical, long-range and local-ordering structural evolution for layered-rocksalt intergrown cathode materials with superior Li storage capability. The intergrown structure is not only limited to the layered-rocksalt phases studied in this work, but can also extend to the spinel phase, which possesses a similar cubic close-packed oxygen structure. Exploring the intergrown structures of layered, rocksalt, and spinel phases opens up more possibilities in the design and development of advanced cathode materials. Each of these phases possess their unique properties: The layered phase offers high capacity, the rocksalt phase contributes to structural stability, and the spinel phase is well known for good ionic conductivity and structural robustness. It should open up a vast array of composition possibilities for high-performance cathode design, moving beyond traditional single-phase materials and offering solutions to longstanding issues like energy density, safety, and cost. This approach would significantly influence the design strategies and performance optimization of next-generation lithium-ion batteries.

Declaration of competing interest

The authors declare that they have no known competing financial interests or personal relationships that could have appeared to influence the work reported in this paper.

Acknowledgment

This work was sponsored by National Natural Science Foundation of China (No. 22109010), National Key R&D Program of China (No. 2021YFC2902905), Beijing Nova Program, Chongqing Outstanding Youth Fund (No. 2022NSCQ-JQX3895), Chongqing Talents Plan for Young Talents (No. CQYC202005032), The Key Project of Chongqing Technology Innovation and Application Development (No. 2022TIAD-DEX0024). N. Li acknowledge the support from Beijing Institute of Technology Research Fund Program for Young Scholars. C. Wei acknowledge the support by the Shanghai Sailing Program (No. 2023×0308–103–01). The authors thank the Beijing Synchrotron Radiation Facility (BSRF) 1W1B for the allocation of synchrotron beamtime and the collection of Ni K-edge spectra. The authors greatly appreciate Taiwan Photon Source (TPS) Beamlines 44A1 and 41A1 for the allocation of synchrotron beamtime, and O K-edge RIXS spectra and Ru K-edge spectra, and local support in data collection and analysis from Prof. Di-Jing Huang, Dr. Chih-Wen Pao, Dr. Hsiao-Yu Huang, Dr. Jun Okamoto, Dr. Amol Singh, and Dr. Jeng-Lung Chen.

Supplementary materials

Supplementary material associated with this article can be found, in the online version, at doi:10.1016/j.cclet.2024.109536.

References

[1] J.M. Paulsen, C.L. Thomas, J.R. Dahn, J. Electrochem. Soc. 146 (1999) 3560–3565.
[2] Z. Lu, D.D. MacNeil, J.R. Dahn, Electrochem. Solid-State Lett. 4 (2001) A191–A194.
[3] Y.K. Sun, M.G. Kim, S.H. Kang, K. Amine, J. Mater. Chem. 13 (2003) 319–322.
[4] J.S. Kim, C.S. Johnson, J.T. Vaughey, et al., Chem. Mater. 16 (2004) 1996–2006.
[5] N. Yabuuchi, K. Yoshii, S.T. Myung, I. Nakai, S. Komaba, J. Am. Chem. Soc. 133 (2011) 4404–4419.
[6] S. Sun, C.Z. Zhao, H. Yuan, et al., Sci. Adv. 8 (2022) eadd5189.
[7] J. Liu, X.W. Mei, F. Peng, Chin. Chem. Lett. 34 (2023) 108187.
[8] D. Mohanty, J. Li, D.P. Abraham, et al., Chem. Mater. 26 (2014) 6272–6280.
[9] W. Zuo, M. Luo, X. Liu, et al., Energy Environ. Sci. 13 (2020) 4450–4497.
[10] L. Xu, S. Chen, Y. Su, et al., Energy Mater. Adv. 4 (2023) 0045.
[11] J.Z. Xiong, Z.C. Yang, X.L. Guo, et al., Tungsten 6 (2024) 174–195.
[12] L.X. Ma, T.D. Chen, C.X. Hai, et al., Tungsten 6 (2024) 259–268.
[13] K. Zhang, Y. Tian, X. Chen, S. Hu, Z. Jian, Chin. Chem. Lett. 35 (2024) 108308.
[14] S. Maiti, H. Sclar, R. Sharma, et al., Adv. Funct. Mater. 31 (2020) 2008083.
[15] M.J. Lee, E. Lho, P. Oh, Y. Son, J. Cho, Nano Res. 10 (2017) 4210–4220.
[16] F. Zheng, C. Yang, X. Xiong, et al., Angew. Chem. Int. Ed. 54 (2015) 13058–13062.
[17] J.Y. Piao, L. Gu, Z. Wei, et al., J. Am. Chem. Soc. 141 (2019) 4900–4907.
[18] Y. Zhao, M. Xia, X. Hu, et al., Electrochim. Acta 174 (2015) 1167–1174.
[19] L. Li, B.H. Song, Y.L. Chang, et al., J. Power Sources 283 (2015) 162–170.
[20] J. Yang, Y. Chen, Y. Li, et al., ACS Appl. Mater. Interfaces 13 (2021) 25981–25992.
[21] E. Wang, D. Xiao, T. Wu, et al., Adv. Funct. Mater. 32 (2022) 2201744.
[22] L. Xu, S. Chen, N. Li, et al., ACS Appl. Energy Mater. 5 (2022) 9970–9979.
[23] L. Xu, S. Chen, Y. Su, et al., ACS Appl. Mater. Interfaces 47 (2023) 54559–54567.
[24] S. Sun, Z. Han, W. Liu, et al., Nat. Commun. 14 (2023) 6662.
[25] F. Wu, N. Li, Y. Su, et al., Adv. Mater. 25 (2013) 3722–3726.
[26] F. Wu, N. Li, Y. Su, et al., Nano Lett. 14 (2014) 3550–3555.
[27] L. Wang, T. Liu, T. Wu, J. Lu, Nature 611 (2022) 61–67.
[28] B. Li, G. Rousse, L. Zhang, et al., Energy Environ. Sci. 16 (2023) 1210–1222.
[29] N. Li, M. Sun, W.H. Kan, et al., Nat. Commun. 12 (2021) 2348.
[30] N. Li, J. Wu, S. Hwang, et al., ACS Energy Lett. 5 (2020) 3535–3543.
[31] B. Li, M.T. Sougrati, G. Rousse, et al., Nat. Chem. 13 (2021) 1070–1080.
[32] J. Hong, W.E. Gent, P. Xiao, et al., Nat. Mater. 18 (2019) 256–265.
[33] B. Li, K. Kumar, I. Roy, et al., Nat. Mater. 21 (2022) 1165–1174.
[34] R.A. House, J.J. Marie, J. Park, et al., Nat. Commun. 12 (2021) 2975.
[35] R.A. House, U. Maitra, M.A. Perez-Osorio, et al., Nature 577 (2020) 502–508.
[36] T. Kim, B. Song, A.J.G. Lunt, et al., Chem. Mater. 28 (2016) 4191–4203.